Signatures of adatom effects in the quasiparticle spectrum of Li-doped graphene

Kristen Kaasbjerg [*] and Antti-Pekka Jauho

Center for Nanostructured Graphene (CNG), Department of Physics, Technical University of Denmark, DK-2800 Kgs. Lyngby, Denmark

We study the spectral function and quasiparticle scattering in Li-decorated graphene (Li@graphene) with an atomistic T-matrix formalism and uncover adatom-induced spectral effects which shed light on experimentally observed angle-resolved photoemission spectroscopy (ARPES) features. From transport studies, alkali adatoms are known to introduce charged-impurity scattering limiting the carrier mobility. Here, we demonstrate that Li adatoms furthermore give rise to a low-energy impurity band centered at the Γ point which originates from the hybridization between the atomic $2s$ state of the Li adatoms and graphene "surface" states. We show that the impurity band is strongly dependent on the concentration c_{Li} of Li adatoms, and aligns with the Li-induced Fermi level on the Dirac cone at $c_{Li} \sim 8\%$ ($E_F \approx 1.1$ eV). Finally, we show that adatom-induced quasiparticle scattering increases dramatically at energies above ~ 1 eV close to the van Hove singularity in the graphene density of states, giving rise to a large linewidth broadening on the Dirac cone with a concomitant downshift and a characteristic kink in the conduction band. Our findings are highly relevant for future studies of ARPES, transport, and superconductivity in adatom-doped graphene.

Introduction. Graphene decorated with metallic adatoms has emerged as an interesting platform for engineering graphene's electronic properties and realizing novel electronic phases such as, e.g., the quantum spin Hall phase [1–3] and superconductivity [4–6]. In addition, doping with adatoms opens the opportunity to probe the electronic properties of graphene at high energies with, e.g., Fermi levels in excess of 1 eV in alkali-doped graphene [7–12]. However, metallic adatoms at the same time introduce charged-impurity scattering, thus limiting the transport in adatom-doped graphene [12–16].

The spectral properties of adatom-doped graphene have been studied with angle-resolved photoemission spectroscopy (ARPES) [17] in several works [7–11,18–20], demonstrating many-body effects such as, e.g., electron-electron and electron-phonon (el-ph) interactions [21–26], while the effect of adatom-induced impurity scattering [12–15] in ARPES is not well understood [20]. In addition, signatures of superconductivity have been observed in ARPES on Li-decorated graphene (Li@graphene) at Li concentrations corresponding to a Fermi level of $E_F \sim 1$ eV [11]. They appeared alongside a spectral feature at the Γ point which in the ordered LiC$_6$ structure [5] and alkali metal-graphite intercalation compounds [27–29] corresponds to a metal-atom dominated band predicted to promote superconductivity [5].

In this Rapid Communication, we study the spectral properties of *disordered* Li@graphene, i.e., graphene with a random configuration of Li adatoms as illustrated in Fig. 1(a), using an atomistic first-principles T-matrix formalism based on a parameter-free description of the impurity potential [30,31]. This allows for a detailed description of (i) the spectral Γ-point feature including its concentration dependence as well

as (ii) the *renormalization* and *linewidth broadening* of the bands due to adatom-induced quasiparticle (QP) scattering.

We find that in disordered Li@graphene, the Γ-point feature corresponds to the hybrid impurity band shown in Fig. 1(b), which originates from the coupling between free-electron-like "surface" states localized in proximity to the graphene layer and the atomic Li $2s$ state as sketched in Fig. 1(a). The impurity band evolves downwards in energy from the position of the Li $2s$ state with increasing c_{Li} and aligns with the Fermi level on the Dirac cone at $c_{Li} \sim 8\%$ ($E_F \approx 1.1$ eV). In agreement with experiments [11], this suggests that conditions favorable for superconductivity may be realized in disordered Li@graphene at concentrations well below the concentration ($c_{Li} = 33\%$) in LiC$_6$ [5].
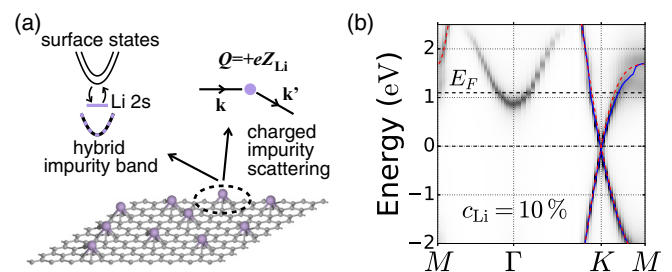

FIG. 1. (a) Atomic illustration of disordered Li@graphene with a random configuration of Li adatoms giving rise to (i) a hybrid impurity band, and (ii) pronounced charged-impurity scattering as sketched in the top part. (b) Spectral function of Li@graphene at a Li concentration of $c_{Li} = 10\%$ showing the appearance of the Γ-point centered hybrid impurity band ~ 0.9 eV above the Dirac point ($E = 0$). The dashed horizontal line indicates the Li-induced Fermi level E_F. The unperturbed Dirac-cone bands (red dashed lines) are renormalized (solid blue lines) and broadened by Li-induced impurity scattering.

*kkaasbjerg@gmail.com

We furthermore analyze the effect of adatom scattering on the Dirac-cone states, and find that charged-impurity scattering dominates the linewidth broadening, while resonant scattering [32–35] by the atomic Li $2s$ state is negligible. Near the M point, the linewidth broadening in Fig. 1(b) increases dramatically due to strong charged-impurity scattering with a concomitant downshift and a kink in the QP band [Fig. 1(b), blue line]. Similar features have been observed at high Fermi energies in different types of metal atom-doped graphene [7,8,10,36], and may yield an artificially high and anisotropic el-ph coupling if attributed entirely to el-ph scattering as pointed out in Refs. [37,38]. As we demonstrate below, adatom-induced impurity scattering presents a non-negligible "intrinsic" contribution to the band renormalization in adatom-doped graphene.

Theory and methods. For a random distribution of Li adatoms as illustrated in Fig. 1(a), the spectral properties probed in ARPES are given by the impurity-averaged Green's function (GF). Here, we apply the atomistic density functional theory (DFT)-based T-matrix formalism described in Refs. [30,31] to calculate the GF for disorderd Li@graphene.

The impurity-averaged Green's function is given by the Dyson equation [39,40]

$$\hat{G}_{\mathbf{k}}^{-1}(\varepsilon) = \hat{G}_{\mathbf{k}}^{0\,-1}(\varepsilon) - \hat{\Sigma}_{\mathbf{k}}(\varepsilon), \qquad (1)$$

where $\mathbf{k} \in$ first Brillouin zone (BZ) and the carets indicate a matrix structure in the band index n. Impurity effects enter via the self-energy $\hat{\Sigma}_{\mathbf{k}}(\varepsilon)$, which modifies the pristine band structure $\varepsilon_{n\mathbf{k}}$ of graphene described by the *noninteracting* Green's function, $G_{n\mathbf{k}}^{0}(\varepsilon) = (\varepsilon - \varepsilon_{n\mathbf{k}} + i\eta)^{-1}$. While $G_{n\mathbf{k}}^{0}$ is diagonal in the band index, the disorder self-energy in (1) is, in general, not diagonal and Eq. (1) must be solved by matrix inversion.

In the T-matrix approximation [40,41], the impurity self-energy is given by $\hat{\Sigma}_{\mathbf{k}}(\varepsilon) = c_i \hat{T}_{\mathbf{kk}}(\varepsilon)$, where $c_i = N_i/N$ is the impurity concentration (impurities per unit cell), and $\hat{T}_{\mathbf{kk}}(\varepsilon)$ denotes the $\mathbf{k}$-diagonal elements of the T matrix. The T matrix takes into account multiple scattering off the individual impurities, and is given by the integral equation

$$\hat{T}_{\mathbf{kk}'}(\varepsilon) = \hat{V}_{\mathbf{kk}'} + \sum_{\mathbf{k}''} \hat{V}_{\mathbf{kk}''} \hat{G}_{\mathbf{k}''}^{0}(\varepsilon) \hat{T}_{\mathbf{k}''\mathbf{k}'}(\varepsilon), \qquad (2)$$

where $\hat{V}_{\mathbf{kk}'}$ are the impurity matrix elements. The T-matrix self-energy is exact to leading order in the impurity concentration c_i, and is therefore a good approximation for low impurity concentration, i.e., $c_i \ll 1$.

In the following, we obtain the GF and spectral function of Li@graphene based on atomistic DFT [linear combination of atomic orbitals (LCAO)] calculations [42] of the band structure and impurity matrix elements sampled in the full BZ using the atomistic method described in Refs. [30,31] (see Ref. [46] for recent related developments).

Li-adatom impurity potential. For the initial characterization of the Li adatoms, we have carried out standard DFT calculations [42], finding that the hollow site at the center of the hexagon of the graphene lattice is the favored adsorption site at a distance of $d = 1.78$ Å above the graphene layer, and a net charge of $Q = -eZ_{\mathrm{Li}}$ donated to the graphene lattice
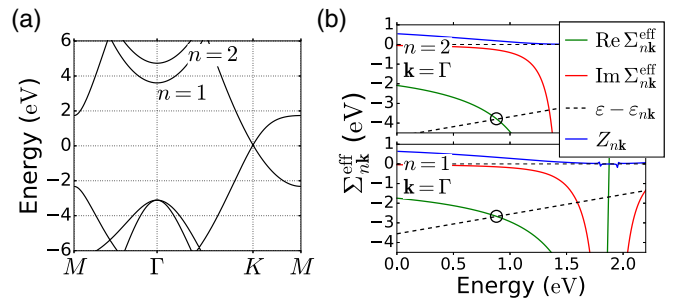

FIG. 2. (a) Graphene band structure featuring two parabolic bands labeled $n = 1, 2$ which are associated with free-electron-like surface states [52]. (b) Diagonal elements of the real and imaginary parts of the effective self-energy in Eq. (5) for the $n = 1, 2$ surface states at $\mathbf{k} = \Gamma$ and $c_{\mathrm{Li}} = 10\%$. The circles indicate the solutions to the QP equation corresponding to the hybrid impurity band in Li@graphene [cf. text below Eq. (4)].

per Li adatom ($Z_{\mathrm{Li}} = +0.9$), consistent with previous works [47,48].

In our DFT calculated impurity matrix elements $V_{\mathbf{kk}'}^{nn'} = \langle \psi_{n\mathbf{k}} | \hat{V}_{\mathrm{Li}} | \psi_{n'\mathbf{k}'} \rangle$ [42], where $|\psi_{n\mathbf{k}}\rangle$ is the Bloch state of the pristine system, the microscopic details of the graphene-Li interaction are encoded in the DFT Li-adatom impurity potential $\hat{V}_{\mathrm{Li}}$. For the sake of simplicity we here express it as

$$\hat{V}_{\mathrm{Li}} = V_C(\hat{\mathbf{r}}) + \sum_{n\mathbf{k}, n'\mathbf{k}'} |\psi_{n\mathbf{k}}\rangle V_{2s,\mathbf{kk}'}^{nn'} \langle \psi_{n'\mathbf{k}'}|, \qquad (3)$$

where the two contributions come from (1) the Coulomb potential $V_C(\mathbf{r})$ from the charged Li adatoms ($Q = +eZ_{\mathrm{Li}}$) which corresponds approximately to a screened point-charge potential given by $V_C(q, d) = e^2 Z_{\mathrm{Li}} e^{-qd}/[2\epsilon_0 q\varepsilon(q)]$ in Fourier space where $\varepsilon(q)$ is the two-dimensional (2D) static dielectric function of graphene [49,50], and (2) the atomic Li $2s$ state with energy E_{2s} which can be reduced to an effective potential $V_{2s,\mathbf{kk}'}^{nn'}$ described by the DFT pseudopotential [31] (see, e.g., Refs [35,51] for tight-binding examples).

For an accurate description of the atomic $2s$ state in the T matrix, we use a Bloch-state basis $\{|\psi_{n\mathbf{k}}\rangle\}$ which describes both the graphene layer and the vacuum region where the Li atoms reside. In our DFT-LCAO based method, this is achieved by introducing so-called "ghost" atoms in the surface region which enlarge the standard LCAO basis for graphene. In the graphene band structure shown in Fig. 2, this gives rise to the two Γ-point centered parabolic bands (labeled $n = 1, 2$) located $\sim$3.5–5 eV above the Dirac point ($E = 0$) which are absent in standard tight-binding and DFT-LCAO calculations [52,53]. The two bands correspond to free-electron-like surface states located predominantly outside the graphene plane with, respectively, even ($n = 1$) and odd ($n = 2$) parity with respect to graphene's mirror symmetry plane [52], and they are instrumental for the occurrence of the impurity band in Fig. 1(b).

Li@graphene spectral function. In Fig. 1(b) we show the calculated spectral function $A_{\mathbf{k}}(\varepsilon) = \sum_n A_{n\mathbf{k}}(\varepsilon)$ for $c_{\mathrm{Li}} = 10\%$, where $A_{n\mathbf{k}}(\varepsilon) = -2\,\mathrm{Im}\,G_{\mathbf{k}}^{nn}(\varepsilon)$ is given by the imaginary part of the diagonal elements of the GF. The dashed horizontal line shows the Fermi level E_F assuming a Li-induced carrier density of $n = Z_{\mathrm{Li}} n_{\mathrm{Li}}$, where n_{Li} is the areal density

of Li atoms, and zero residual doping which is often present experimentally [11]. The spectral function exhibits two distinct features which are absent in the pristine band structure of graphene shown in Fig. 2(a).

The first is the appearance of a prominent Γ-centered parabolic impurity band which starts $\sim$0.9 eV above the Dirac point and extends up to $\sim$2.5 eV where it vanishes. As indicated by the Fermi level, this band is populated at the considered c_{Li} and is hence important for the electronic and transport properties of Li@graphene, including its potential superconducting state [11]. The second feature is a pronounced renormalization and broadening of the conduction band near the M point which is an indication of strong QP scattering.

As justified below, these features can be analyzed using a diagonal form of the impurity-averaged GF, $G_{n\mathbf{k}}(\varepsilon) = [\varepsilon - \varepsilon_{n\mathbf{k}} - \Sigma_{n\mathbf{k}}(\varepsilon)]^{-1}$. Thus, the renormalized QP bands $\tilde{\varepsilon}_{n\mathbf{k}}$ follow from the solution to the QP equation $\varepsilon - \varepsilon_{n\mathbf{k}} - \text{Re}\,\Sigma_{n\mathbf{k}}(\varepsilon) = 0$. In the vicinity of $\tilde{\varepsilon}_{n\mathbf{k}}$, the spectral function takes the form

$$A_{n\mathbf{k}}(\varepsilon) = Z_{n\mathbf{k}} \frac{\gamma_{n\mathbf{k}}}{(\varepsilon - \tilde{\varepsilon}_{n\mathbf{k}})^2 + (\gamma_{n\mathbf{k}}/2)^2}, \quad (4)$$

where the wave-function renormalization, or QP weight, is given by $Z_{n\mathbf{k}} = [1 - \partial_\varepsilon \text{Re}\,\Sigma_{n\mathbf{k}}|_{\varepsilon = \tilde{\varepsilon}_{n\mathbf{k}}}]^{-1}$, and $\gamma_{n\mathbf{k}} = -2Z_{n\mathbf{k}} \text{Im}\,\Sigma_{n\mathbf{k}}|_{\varepsilon = \tilde{\varepsilon}_{n\mathbf{k}}}$ is the linewidth broadening due to impurity scattering.

Besides renormalization of the pristine band structure, impurities with resonant atomic levels may introduce new spectral bands as is the case here. Such features stem from additional solutions $\tilde{\varepsilon}_{\text{imp},\mathbf{k}}$ to the QP equation, and the spectral function acquires an additional impurity component, $A_{n\mathbf{k}}(\varepsilon) \approx 2\pi Z_{n\mathbf{k}} \delta(\varepsilon - \tilde{\varepsilon}_{n\mathbf{k}}) + A_{n\mathbf{k}}^{\text{imp}}(\varepsilon)$, where well-defined QPs are assumed and $A_{n\mathbf{k}}^{\text{imp}}$ is given by Eq. (4) with $\tilde{\varepsilon}_{n\mathbf{k}} \to \tilde{\varepsilon}_{\text{imp},\mathbf{k}}$. By virtue of the sum rule $\int \frac{d\varepsilon}{2\pi} A_{n\mathbf{k}}(\varepsilon) = 1$, this results in a reduction of the QP weights of the pristine bands from their unperturbed value $Z_{n\mathbf{k}} = 1$.

In the rest of this Rapid Communication, we clarify the microscopic origin of the adatom-related features in Fig. 1(b) as well as their dependence on the concentration of Li adatoms.

Hybrid impurity band. The origin of the Γ-centered impurity band can be traced back to the coupling between the $n = 1, 2$ surface states in Fig. 2 and the atomic Li 2s state via the second term in Eq. (3). This introduces a pole in the T matrix at the renormalized energy $\tilde{E}_{2s} \approx 2.55$ eV of the 2s state. At $\mathbf{k} \sim \Gamma$, the pole together with the broken mirror plane symmetry in Li@graphene gives rise to large diagonal and off-diagonal T-matrix elements between the $n = 1, 2$ surface states [54], which dominate all other elements. To facilitate a simple analysis, we can thus approximate the GF in the $n = 1, 2$ surface-state subspace by the inverse of its 2×2 subblock on the right-hand side of Eq. (1). The diagonal elements of the GF take the form $G_{n\mathbf{k}}(\varepsilon) = [\varepsilon - \varepsilon_{n\mathbf{k}} - \Sigma_{n\mathbf{k}}^{\text{eff}}(\varepsilon)]^{-1}$, where the *effective* self-energy,

$$\Sigma_{n\mathbf{k}}^{\text{eff}}(\varepsilon) = \Sigma_{\mathbf{k}}^{nn}(\varepsilon) + \frac{\Sigma_{\mathbf{k}}^{n\bar{n}}(\varepsilon) \Sigma_{\mathbf{k}}^{\bar{n}n}(\varepsilon)}{\varepsilon - \varepsilon_{\bar{n}\mathbf{k}} - \Sigma_{\mathbf{k}}^{\bar{n}\bar{n}}(\varepsilon)}, \quad \bar{n} \neq n, \quad (5)$$

describes virtual transitions between the surface state n and the Li 2s state either (i) directly (first term), or (ii) via the other surface state $\bar{n}$ (second term).
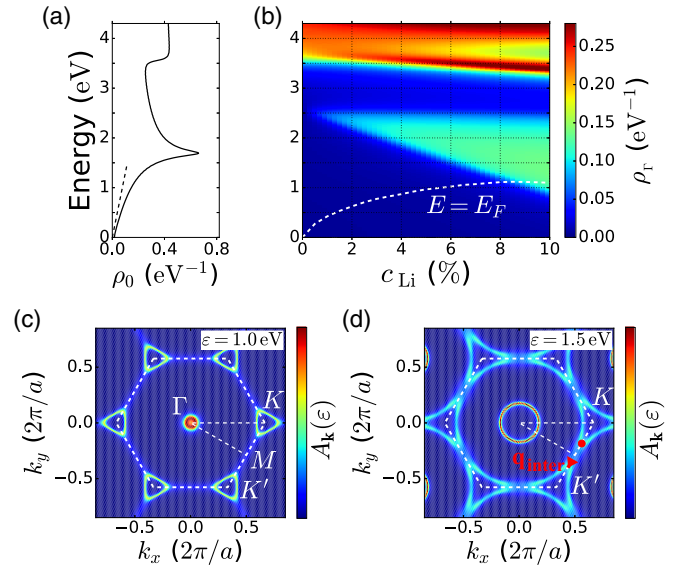

FIG. 3. (a) Density of states of pristine graphene with the dashed line showing the linear DOS in the Dirac model. (b) DOS of the Γ-centered bands in Li@graphene as a function of the Li concentration and energy. The dashed line denotes the Li-induced Fermi level assuming zero residual doping. The constant DOS which develops with increasing c_{Li} in the energy range $\sim$0.9–2.5 eV is due to the hybrid impurity band in Fig. 1(b). (c) and (d) Spectral function at, respectively, $\varepsilon = 1.0$ eV and $\varepsilon = 1.5$ eV for $c_{Li} = 10\%$. In (d), the strong trigonal warping results in a large reduction of the intervalley scattering wave vector (red arrow).

With this form of the diagonal elements of the GF, the analysis in Eq. (4) applies. In Fig. 2(b) we show the real (green lines) and imaginary parts (red lines) of the diagonal elements of the effective self-energy $\Sigma_{n\mathbf{k}}^{\text{eff}}$, together with the calculated QP weight $Z_{n\mathbf{k}}$ (blue lines) and $\varepsilon - \varepsilon_{n\mathbf{k}}$ (black dashed). The intersection of the latter with $\text{Re}\,\Sigma_{n\mathbf{k}}^{\text{eff}}$ (marked with circles) signifies the emergence of the Γ-centered hybrid impurity band in Fig. 1(b). The QP weights at the Γ point are, respectively, $Z_{1\Gamma} \approx 0.3$ and $Z_{2\Gamma} \approx 0.2$, yielding a total QP weight of $Z_{\text{imp},\Gamma} \sim 0.5$ for the impurity band.

We have thus identified the spectral Γ-point feature observed in ARPES [11] as a low-energy hybridized impurity band arising from the coherent coupling between the surface states and the Li 2s state as described by Eq. (5). In the periodic LiC$_6$ structure, the analog of this band plays a pivotal role for the predicted superconductivity by enhancing the el-ph coupling at the Fermi level [5].

It is therefore interesting to investigate the concentration dependence of the impurity band and its alignment with the Fermi level in Li@graphene. In Figs. 3(a) and 3(b), we show the DOS (per unit cell) $\rho(\varepsilon) = -\frac{1}{N\pi} \text{Im}[\text{Tr}\,\hat{G}_{\mathbf{k}}(\varepsilon)]$ for, respectively, (i) pristine graphene (ρ_0), and (ii) the Γ-centered bands in Li@graphene (ρ_Γ) obtained by restricting the $\mathbf{k}$ sum in the trace to a region around the Γ point enclosing the relevant bands. The dashed line in Fig. 3(b) marks the position of the Fermi level corresponding to the Li-induced carrier density $n = Z_{Li} n_{Li}$. In the Dirac model the Fermi energy scales as $E_F = \hbar v_F \sqrt{\pi Z_{Li} n_{Li}} \approx 120 \sqrt{n/(10^{12}\,\text{cm}^{-2})}$ meV, whereas the Fermi energy in Fig. 3(b) deviates from this
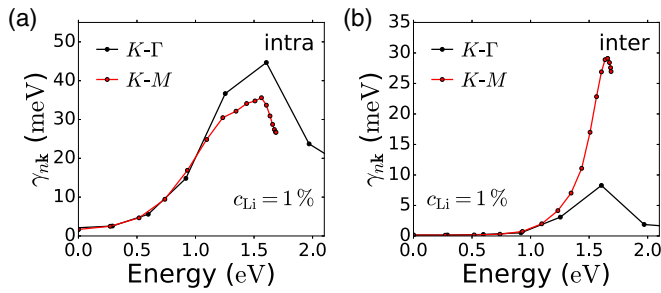
FIG. 4. Adatom-induced linewidth broadening $\gamma_{n\mathbf{k}}$, or QP scattering rate $\tau_{n\mathbf{k}}^{-1} = \gamma_{n\mathbf{k}}/\hbar$, in the conduction band as a function of the on-shell energy $\tilde{\varepsilon}_{n\mathbf{k}}$ (along the indicated BZ paths) at $c_{\mathrm{Li}} = 1\%$. The total broadening has been split up into contributions from (a) intravalley and (b) intervalley scattering, respectively. The peaks in the linewidth broadening correlate with the position of the vHS in the DOS in Fig. 3(a).

square-root dependence at high c_{Li} where it flattens out due to the population of the hybrid band and the nonlinear part of the Dirac cone. The figure illustrates the development of the hybrid impurity band which starts from the position of the Li $2s$ state $\tilde{E}_{2s}$ and moves down towards the Dirac cone with increasing Li concentration. Interestingly, our calculations show that the hybrid impurity band aligns with the Fermi level on the Dirac cone at Li concentrations as low as $c_{\mathrm{Li}} \sim 8\%$ ($E_F \approx 1.1$ eV) where the DOS ρ_Γ of the impurity band and the Dirac-cone DOS ρ_0 are comparable. In the presence of a residual doping of graphene [11], this situation is realized at even lower c_{Li}.

Dirac-cone QP properties. Finally, we consider the effect of adatom-induced QP scattering on the renormalization and linewidth broadening of the Dirac-cone bands in Fig. 1(b) and Figs. 3(c) and 3(d). As the self-energy on the Dirac cone is diagonal [54], the renormalized QP bands $\tilde{\varepsilon}_{n\mathbf{k}}$ and linewidth broadening $\gamma_{n\mathbf{k}}$ can be obtained as explained above and below Eq. (4).

In Fig. 4 we show the energy dependence of the linewidth broadening of the conduction band along the K-Γ and K-M paths for a fixed Li concentration of $c_{\mathrm{Li}} = 1\%$ at which the impurity band is absent [cf. Fig. 3(a)]. For clarity, we have separated out the contributions from intravalley (left) and intervalley (right) scattering using the optical theorem [31,54]. At energies below ~ 1 eV, the intravalley rate exceeds the intervalley rate by far. This is consistent with charged-impurity scattering where intervalley scattering with $q \approx |\mathbf{K} - \mathbf{K}'|$ is weak due to the q dependence of the 2D Coulomb potential $V_C(q, d)$. We find no indications of resonant scattering [32–35] which is suppressed by the remote energy $\tilde{E}_{2s}$ of the Li $2s$ state as well as the invisibility of short-range impurity potentials due to adatoms in the hollow site [35,55,56]. At higher energies, both the intra- and intervalley rates increase dramatically and peak at the energy $\varepsilon \approx 1.75$ eV of the van

Hove singularity (vHS) in the DOS in Fig. 3(a). Whereas the increasing DOS at the vHS is the main reason for the increasing intravalley rate, also the strong trigonal warping of the Dirac cones seen in Figs. 3(c) and 3(d) is important in order to explain the increase in the intervalley rate. As illustrated in Fig. 3(d), the trigonal warping reduces the intervalley scattering wave vector markedly and thereby enhances the scattering probability due to the q dependence of Coulomb potential. This effect is most pronounced on the K-M path, where the reduction in the $K \rightarrow K'$ intervalley wave vector is strongest, and results in an anisotropic linewidth broadening also visible on the $\varepsilon = 1.5$ eV constant-energy contours in Fig. 3(d). In Figs. 3(c) and 3(d), $c_{\mathrm{Li}} = 10\%$, and $\Gamma \leftrightarrow K$ scattering between the overlapping impurity band and Dirac cones may also contribute to the broadening. However, the narrow linewidth of the impurity band shows that this scattering channel is weak because of a small impurity matrix element between the spatially separated surface and Dirac-cone states. Dirac-cone QP scattering is thus not affected markedly by the impurity band.

Interestingly, the strong peak in the linewidth broadening at the vHS is accompanied by a pronounced renormalization of the conduction band in the same energy range as demonstrated by the calculated QP band in Fig. 1(b) (solid blue line). Along the K-M path, the conduction band exhibits a pronounced downshift and a kink ~ 100–200 meV below the vHS, resembling experimental ARPES features in highly adatom-doped [8,10] as well as intercalated [36] graphene. At high doping levels [7,8,10], this adatom-induced kink may interfere with el-ph related kinks located at the optical phonon energy ~ 200 meV below the Fermi level [21–23,26], thus obscuring the analysis of the el-ph interaction [37,38] in the regime relevant for superconductivity.

Conclusions. We have studied the spectral function and quasiparticle scattering in disordered Li-decorated graphene with an atomistic T-matrix method. We demonstrate that (i) the experimentally observed low-energy spectral feature at the Γ point [11] originates from a Li-dependent hybrid impurity band which aligns with the Li-induced Fermi level at $c_{\mathrm{Li}} \approx 8\%$, and (ii) Li-induced charged-impurity scattering produces a strong linewidth broadening and a concomitant downshift and kink in the conduction band in the vicinity of the van Hove singularity in the graphene DOS. Our findings are highly relevant for future studies of transport [12–15] and ARPES [8,10,36] as well as analyses of the el-ph interaction [37,38] and superconductivity [5,11] in adatom-doped graphene.

[1] C. Weeks, J. Hu, J. Alicea, M. Franz, and R. Wu, Engineering a Robust Quantum Spin Hall State in Graphene via Adatom Deposition, Phys. Rev. X **1**, 021001 (2011).

[2] A. Cresti, D. Van Tuan, D. Soriano, A. W. Cummings, and S. Roche, Multiple Quantum Phases in Graphene with Enhanced Spin-Orbit Coupling: From the Quantum Spin Hall Regime to

the Spin Hall Effect and a Robust Metallic State, Phys. Rev. Lett. **113**, 246603 (2014).

[3] F. J. Santos, D. A. Bahamon, R. B. Muniz, K. McKenna, E. V. Castro, J. Lischner, and A. Ferreira, Impact of complex adatom-induced interactions on quantum spin Hall phases, Phys. Rev. B **98**, 081407(R) (2018).

[4] B. Uchoa and A. H. Castro Neto, Superconducting States of Pure and Doped Graphene, Phys. Rev. Lett. **98**, 146801 (2007).

[5] G. Profeta, M. Calandra, and F. Mauri, Phonon-mediated super-conductivity in graphene by lithium deposition, Nat. Phys. **8**, 131 (2012).

[6] E. R. Margine and F. Giustino, Two-gap superconductivity in heavily *n*-doped graphene: *Ab initio* Migdal-Eliashberg theory, Phys. Rev. B **90**, 014518 (2014).

[7] M. Bianchi, E. D. L. Rienks, S. Lizzit, A. Baraldi, R. Balog, L. Hornekær, and P. Hofmann, Electron-phonon coupling in potassium-doped graphene: Angle-resolved photoemission spectroscopy, Phys. Rev. B **81**, 041403(R) (2010).

[8] J. L. McChesney, A. Bostwick, T. Ohta, T. Seyller, K. Horn, J. González, and E. Rotenberg, Extended van Hove Singularity and Superconducting Instability in Doped Graphene, Phys. Rev. Lett. **104**, 136803 (2010).

[9] D. A. Siegel, C.-H. Park, C. Hwang, J. Deslippe, A. V. Fedorov, S. G. Louie, and A. Lanzara, Many-body interactions in quasi-freestanding graphene, Proc. Natl. Acad. Sci. USA **108**, 11365 (2011).

[10] A. V. Fedorov, N. I. Verbitskiy, D. Haberer, C. Struzzi, L. Petaccia, D. Usachov, O. Y. Vilkov, D. V. Vyalikh, J. Fink, M. Knupfer, B. Büchner, and A. Grüneis, Observation of a universal donor-dependent vibrational mode in graphene, Nat. Commun. **5**, 3257 (2014).

[11] B. M. Ludbrook, G. Levy, P. Nigge, M. Zonno, M. Schneider, D. J. Dvorak, C. N. Veenstra, S. Zhdanovich, D. Wong, P. Dosanjh, C. Straßer, A. Stöhr, S. Forti, C. R. Ast, U. Starke, and A. Damascelli, Evidence for superconductivity in Li-decorated monolayer graphene, Proc. Natl. Acad. Sci. USA **112**, 11795 (2015).

[12] A. Khademi, E. Sajadi, P. Dosanjh, D. A. Bonn, J. A. Folk, A. Stöhr, U. Starke, and S. Forti, Alkali doping of graphene: The crucial role of high-temperature annealing, Phys. Rev. B **94**, 201405(R) (2016).

[13] J.-H. Chen, C. Jang, S. Adam, M. S. Fuhrer, E. D. Williams, and M. Ishigami, Charged-impurity scattering in graphene, Nat. Phys. **4**, 377 (2008).

[14] J. Yan and M. S. Fuhrer, Correlated Charged Impurity Scattering in Graphene, Phys. Rev. Lett. **107**, 206601 (2011).

[15] U. Chandni, E. A. Henriksen, and J. P. Eisenstein, Transport in indium-decorated graphene, Phys. Rev. B **91**, 245402 (2015).

[16] A. Khademi, K. Kaasbjerg, P. Dosanjh, A. Stöhr, S. Forti, U. Starke, and J. A. Folk, Weak localization measurements of electronic scattering rates in Li-doped epitaxial graphene, Phys. Rev. B **100**, 161405(R) (2019).

[17] A. Damascelli, Z. Hussain, and Z.-X. Shen, Angle-resolved photoemission studies of the cuprate superconductors, Rev. Mod. Phys. **75**, 473 (2003).

[18] A. Bostwick, T. Ohta, T. Seyller, K. Horn, and E. Rotenberg, Quasiparticle dynamics in graphene, Nat. Phys. **3**, 36 (2007).

[19] D. A. Siegel, W. Regan, A. V. Fedorov, A. Zettl, and A. Lanzara, Charge-Carrier Screening in Single-Layer Graphene, Phys. Rev. Lett. **110**, 146802 (2013).

[20] C. Straßer, B. M. Ludbrook, G. Levy, A. J. Macdonald, S. A. Burke, T. O. Wehling, K. Kern, A. Damascelli, and C. R. Ast, Long-versus short-range scattering in doped epitaxial graphene, Nano Lett. **15**, 2825 (2015).

[21] M. Calandra and F. Mauri, Electron-phonon coupling and electron self-energy in electron-doped graphene: Calculation of angular-resolved photoemission spectra, Phys. Rev. B **76**, 205411 (2007).

[22] C. H. Park, F. Giustino, M. L. Cohen, and S. G. Louie, Velocity Renormalization and Carrier Lifetime in Graphene from the Electron-Phonon Interaction, Phys. Rev. Lett. **99**, 086804 (2007).

[23] W. K. Tse and S. Das Sarma, Phonon-Induced Many-Body Renormalization of the Electronic Properties of Graphene, Phys. Rev. Lett. **99**, 236802 (2007).

[24] E. H. Hwang and S. Das Sarma, Quasiparticle spectral function in doped graphene: Electron-electron interaction effects in ARPES, Phys. Rev. B **77**, 081412(R) (2008).

[25] M. Polini, R. Asgari, G. Borghi, Y. Barlas, T. Pereg-Barnea, and A. H. MacDonald, Plasmons and the spectral function of graphene, Phys. Rev. B **77**, 081411(R) (2008).

[26] C.-H. Park, F. Giustino, C. D. Spataru, M. L. Cohen, and S. G. Louie, Angle-resolved photoemission spectra of graphene from first-principles calculations, Nano. Lett. **9**, 4234 (2009).

[27] G. Csányi, P. B. Littlewood, A. H. Nevidomskyy, C. J. Pickard, and B. D. Simons, The role of the interlayer state in the electronic structure of superconducting graphite intercalated compounds, Nat. Phys. **1**, 42 (2005).

[28] M. Calandra and F. Mauri, Theoretical Explanation of Superconductivity in C_6Ca, Phys. Rev. Lett. **95**, 237002 (2005).

[29] J. Chapman, Y. Su, C. A. Howard, D. Kundys, A. N. Grigorenko, F. Guinea, A. K. Geim, I. V. Grigorieva, and R. R. Nair, Superconductivity in Ca-doped graphene laminates, Sci. Rep. **6**, 23254 (2016).

[30] K. Kaasbjerg, J. H. J. Martiny, T. Low, and A.-P. Jauho, Symmetry-forbidden intervalley scattering by atomic defects in monolayer transition-metal dichalcogenides, Phys. Rev. B **96**, 241411(R) (2017).

[31] K. Kaasbjerg, Atomistic *T*-matrix theory of disordered 2D materials: Bound states, spectral properties, quasiparticle scattering and transport, arXiv:1911.00530.

[32] D. M. Basko, Resonant low-energy electron scattering on short-range impurities in graphene, Phys. Rev. B **78**, 115432 (2008).

[33] J. P. Robinson, H. Schomerus, L. Oroszlány, and V. I. Fal'ko, Adsorbate-Limited Conductivity of Graphene, Phys. Rev. Lett. **101**, 196803 (2008).

[34] T. O. Wehling, S. Yuan, A. I. Lichtenstein, A. K. Geim, and M. I. Katsnelson, Resonant Scattering by Realistic Impurities in Graphene, Phys. Rev. Lett. **105**, 056802 (2010).

[35] S. Irmer, D. Kochan, J. Lee, and J. Fabian, Resonant scattering due to adatoms in graphene: Top, bridge, and hollow positions, Phys. Rev. B **97**, 075417 (2018).

[36] S. Link, S. Forti, A. Stöhr, K. Küster, M. Rösner, D. Hirschmeier, C. Chen, J. Avila, M. C. Asensio, A. A. Zakharov, T. O. Wehling, A. I. Lichtenstein, M. I. Katsnelson, and U. Starke, Introducing strong correlation effects into graphene by gadolinium intercalation, Phys. Rev. B **100**, 121407(R) (2019).

[37] C.-H. Park, F. Giustino, J. L. McChesney, A. Bostwick, T. Ohta, E. Rotenberg, M. L. Cohen, and S. G. Louie, van Hove singularity and apparent anisotropy in the electron-phonon interaction in graphene, Phys. Rev. B **77**, 113410 (2008).

[38] M. Calandra and F. Mauri, Electronic structure of heavily doped graphene: The role of foreign atom states, Phys. Rev. B **76**, 161406(R) (2007).

[39] G. D. Mahan, *Many-Particle Physics*, 3rd ed. (Springer, Berlin, 2010).

[40] H. Bruus and K. Flensberg, *Many-Body Quantum Theory in Condensed Matter Physics* (Oxford University Press, Oxford, U.K., 2004).

[41] J. Rammer, *Quantum Transport Theory* (Perseus Books, New York, 1998).

[42] All DFT calculations have been performed with the electronic structure code GPAW [43–45] within the projector augmented-wave method, using the local density approximation (LDA) exchange-correlation (xc) functional and a LCAO double-zeta polarized (DZP) basis set. The ground-state calculation of the optimized structure and Bloch functions was performed using a 21×21 **k**-point sampling of the BZ. The Li impurity potential was obtained using a 11×11 supercell and a 3×3 **k**-point sampling. All calculations include 10 Å of vacuum between graphene and the cell boundaries in the vertical direction imposed with Dirichlet boundary conditions. The impurity matrix elements, T-matrix self-energy and GF were obtained on a 54×54 BZ grid, including the 12 lowest bands and using a numerical broadening of $\eta = 100$ meV.

[43] J. J. Mortensen, L. B. Hansen, and K. W. Jacobsen, Real-space grid implementation of the projector augmented wave method, Phys. Rev. B **71**, 035109 (2005).

[44] A. H. Larsen, M. Vanin, J. J. Mortensen, K. S. Thygesen, and K. W. Jacobsen, Localized atomic basis set in the projector augmented wave method, Phys. Rev. B **80**, 195112 (2009).

[45] J. Enkovaara, C. Rostgaard, J. J. Mortensen, J. Chen, M. Dułak, L. Ferrighi, J. Gavnholt, C. Glinsvad, V. Haikola, H. A. Hansen *et al.*, Electronic structure calculations with GPAW: A real-space implementation of the projector augmented-wave method, J. Phys.: Condens. Matter **22**, 253202 (2010).

[46] I.-T. Lu, J.-J. Zhou, and M. Bernardi, Efficient *ab initio* calculations of electron-defect scattering and defect-limited carrier mobility, Phys. Rev. Mater. **3**, 033804 (2019).

[47] K. T. Chan, J. B. Neaton, and M. L. Cohen, First-principles study of metal adatom adsorption on graphene, Phys. Rev. B **77**, 235430 (2008).

[48] T. O. Wehling, M. I. Katsnelson, and A. I. Lichtenstein, Impurities on graphene: Midgap states and migration barriers, Phys. Rev. B **80**, 085428 (2009).

[49] E. H. Hwang, S. Adam, and S. Das Sarma, Carrier Transport in Two-Dimensional Graphene Layers, Phys. Rev. Lett. **98**, 186806 (2007).

[50] Here, screening of the impurity potential by the Li-induced carriers is accounted for in the supercell DFT calculation of the impurity potential corresponding to a Fermi energy of $E_F = 0.5$ eV.

[51] T. O. Wehling, M. I. Katsnelson, and A. I. Lichtenstein, Adsorbates on graphene: Impurity states and electron scattering, Chem. Phys. Lett. **476**, 125 (2009).

[52] N. R. Papior, G. Calogero, and M. Brandbyge, Simple and efficient LCAO basis sets for the diffuse states in carbon nanostructures, J. Phys.: Condens. Matter **30**, 25LT01 (2018).

[53] A. H. Castro Neto, F. Guinea, N. M. R. Peres, K. S. Novoselov, and A. K. Geim, The electronic properties of graphene, Rev. Mod. Phys. **81**, 109 (2009).

[54] See Supplemental Material at http://link.aps.org/supplemental/10.1103/PhysRevB.100.241405 for plots of the T-matrix self-energy and details on the extraction of the intra- and intervalley contributions to the linewidth broadening using the optical theorem.

[55] J. Duffy, J. Lawlor, C. Lewenkopf, and M. S. Ferreira, Impurity invisibility in graphene: Symmetry guidelines for the design of efficient sensors, Phys. Rev. B **94**, 045417 (2016).

[56] D. A. Ruiz-Tijerina and L. G. G. V. D. da Silva, Symmetry-protected coherent transport for diluted vacancies and adatoms in graphene, Phys. Rev. B **94**, 085425 (2016).